

Sunyaev–Zel’dovich profile fitting with joint AMI-*Planck* analysis

Yvette C. Perrott^{1,2*}, Kamran Javid¹, Pedro Carvalho³, Patrick J. Elwood¹,
Michael P. Hobson¹, Anthony N. Lasenby^{1,4}, Malak Olamaie^{1,5},
and Richard D. E. Saunders^{1,4}

¹*Astrophysics Group, Cavendish Laboratory, JJ Thomson Avenue, Cambridge CB3 0HE, UK*

²*School of Chemical and Physical Sciences, Victoria University of Wellington, PO Box 600, Wellington 6140, New Zealand*

³*Cambridge Machines Deep Learning and Bayesian Systems (CMDLABS) Ltd, 22 Wycombe End, Beaconsfield, Buckinghamshire, United Kingdom, HP9 1NB*

⁴*Kavli Institute for Cosmology Cambridge, Madingley Road, Cambridge, CB3 0HA, UK*

⁵*Imperial Centre for Inference and Cosmology (ICIC), Imperial College, Prince Consort Road, London SW7 2AZ, UK*

Accepted XXX. Received YYY; in original form ZZZ

ABSTRACT

We develop a Bayesian method of analysing Sunyaev-Zel’dovich measurements of galaxy clusters obtained from the Arcminute Microkelvin Imager (AMI) radio interferometer system and from the *Planck* satellite, using a joint likelihood function for the data from both instruments. Our method is applicable to any combination of *Planck* data with interferometric data from one or more arrays. We apply the analysis to simulated clusters and find that when the cluster pressure profile is known a-priori, the joint dataset provides precise and accurate constraints on the cluster parameters, removing the need for external information to reduce the parameter degeneracy. When the pressure profile deviates from that assumed for the fit, the constraints become biased. Allowing the pressure profile shape parameters to vary in the analysis allows an unbiased recovery of the integrated cluster signal and produces constraints on some shape parameters, depending on the angular size of the cluster. When applied to real data from *Planck*-detected cluster PSZ2 G063.80+11.42, our method resolves the discrepancy between the AMI and *Planck* *Y*-estimates and usefully constrains the gas pressure profile shape parameters at intermediate and large radii.

Key words: methods: data analysis – galaxies: clusters: general – galaxies: clusters: individual: PSZ2 G063.80+11.42 – galaxies: clusters: intracluster medium – cosmology: observations.

1 INTRODUCTION

With the advent of large Sunyaev-Zel’dovich (SZ) effect surveys carried out by instruments such as *Planck* (Planck Collaboration et al. 2016), the Atacama Cosmology Telescope (Hilton et al. 2018), and the South Pole Telescope (Bleem et al. 2015), SZ observations have the potential to become a powerful tool for constraining, for example, cosmological properties via cluster number counts. Numerical simulations show a tight, low-scatter correlation between the SZ observable, the Compton- γ parameter and cluster mass (e.g. da Silva et al. 2004, Nagai 2006), but recent attempts to use SZ cluster number counts for cosmological analysis have produced results in tension with other, more mature methods such as the Cosmic Microwave Background (CMB) primary anisotropies (Planck Collaboration et al. 2016). One issue is the uncertain mass-observable calibration, although another issue is the modelling of the observable itself.

Perrott et al. (2015) (hereafter P15) compared properties of 99 galaxy clusters observed in SZ with *Planck* and the Arcminute Mi-

crokelvin Imager (AMI) radio interferometer system. They showed that the discrepancies between the cluster parameters as constrained by AMI and *Planck* could be explained by the cluster gas pressure profile deviating from the profile assumed for analysis. The AMI observations were shown to be particularly sensitive to this effect when attempting to constrain the total integrated Compton- γ parameter due to missing angular scales. It was noted in P15 that the combination of the two instruments would be powerful for investigating the gas pressure profiles of the clusters due to the complementary angular scales measured. In this paper we explore this idea further by developing a joint Bayesian analysis pipeline which combines the data from the two instruments. We note that this pipeline could also be used with other interferometric data, for example from the Atacama Large Millimeter/submillimeter Array (ALMA) which has recently been used for SZ analysis (e.g. Kitayama et al. 2016) and in the future for the Square Kilometre Array (SKA), which will be able to observe the SZ effect in its highest frequency band (Grainge et al. 2015). The pipeline would also be easily extended to include data from other single-dish instruments such as NIKA(2) (e.g. Adam et al. 2014). This work joins a growing body of analysis combining SZ data from different instruments, sensitive to different angular scales.

* E-mail: yvette.perrott@vuw.ac.nz

Recent work such as [Sayers et al. \(2016\)](#), [Ruppin et al. \(2017\)](#), and [Di Mascolo et al. \(2019\)](#) all combine Planck Modified Internal Linear Combination Algorithm (MILCA; [Planck Collaboration et al. 2016](#)) y -maps with SZ data from other instruments to jointly fit the gas pressure profile, while [Romero et al. \(2018\)](#) use a Planck-derived prior on the integrated Compton- y parameter; however to our knowledge this is the first time that Planck frequency maps (rather than y -maps) have been jointly analysed with other SZ data.

The paper is arranged as follows. In Section 2 we describe the telescopes and data used in our analysis and in Section 3 we describe our analysis method. In Section 4 we describe our cluster model. In Sections 5 and 6 we verify our method using simulated clusters and in Section 7 we apply the method to a test case using real data. We anticipate further work in Section 8 and conclude in Section 9.

2 PLANCK AND AMI TELESCOPES

2.1 Planck satellite

The combination of the *Planck* satellite’s low-frequency and high-frequency instruments (LFI and HFI) provides nine frequency channels in the range 37 GHz – 857 GHz. The HFI, used for cluster analysis, has angular resolutions of 10, 7.1, and 5.5 arcminutes at 100, 143, and 217 GHz and 5.0 arcminutes at each of 353, 545, and 857 GHz. The *Planck* frequency bands correspond to two decrements, the null, and three increments in the SZ spectrum, making it particularly effective at the blind identification of galaxy clusters despite its relatively low angular resolution. See e.g. [Planck Collaboration et al. 2016](#) for further details.

2.2 AMI

AMI ([Zwart et al. 2008](#)) is a dual-array interferometer designed for SZ studies, which is situated near Cambridge, UK. AMI consists of two arrays: the Small Array (SA), optimised for viewing arcminute-scale features, having an angular resolution of ≈ 3 arcmin and sensitivity to structures up to ≈ 10 arcmin in scale; and the Large Array (LA), with angular resolution of ≈ 30 arcsec, which is insensitive to SA angular scales and is used to characterise and subtract confusing radio-sources. Both arrays operate over the same frequency band with a central frequency of ≈ 15.5 GHz and a bandwidth of ≈ 5 GHz; in P15 this was divided into 6 channels but after a recent correlator upgrade the band is now divided into 4096 channels ([Hickish et al. 2018](#)), and binned down to 8 channels for analysis after radio-frequency-interference excision and calibration. The simulated data in this paper have the properties of the new correlator.

3 JOINT LIKELIHOOD ANALYSIS

3.1 Bayesian parameter estimation

For a model, \mathcal{M} and a data vector, \mathcal{D} , we can obtain the probability distributions of model parameters (also known as input or sampling parameters) $\boldsymbol{\theta}$ conditioned on \mathcal{M} and \mathcal{D} using Bayes’ theorem:

$$Pr(\boldsymbol{\theta}|\mathcal{D}, \mathcal{M}) = \frac{Pr(\mathcal{D}|\boldsymbol{\theta}, \mathcal{M}) Pr(\boldsymbol{\theta}|\mathcal{M})}{Pr(\mathcal{D}|\mathcal{M})}, \quad (1)$$

where $Pr(\boldsymbol{\theta}|\mathcal{D}, \mathcal{M}) \equiv \mathcal{P}(\boldsymbol{\theta})$ is the posterior distribution of the model parameter set, $Pr(\mathcal{D}|\boldsymbol{\theta}, \mathcal{M}) \equiv \mathcal{L}(\boldsymbol{\theta})$ is the likelihood function for the data, $Pr(\boldsymbol{\theta}|\mathcal{M}) \equiv \pi(\boldsymbol{\theta})$ is the prior probability distribution for the model parameter set, and $Pr(\mathcal{D}|\mathcal{M}) \equiv \mathcal{Z}(\mathcal{D})$ is the

Bayesian evidence of the data given a model \mathcal{M} . In this paper we will be interested in the posterior distributions of the sampling parameters rather than the evidence, which would be used for model comparison. We use the nested sampling algorithm MULTINEST ([Feroz et al. 2009](#)) to calculate our posteriors.

3.2 Model parameters

The model parameters can be split into two subsets (which are assumed to be independent of one another): cluster parameters $\boldsymbol{\theta}_{\text{cl}}$ and radio-source or ‘nuisance’ parameters $\boldsymbol{\theta}_{\text{rs}}$. The cluster model parameters are relevant to both AMI and *Planck* data, and are detailed with their associated priors $\pi(\boldsymbol{\theta}_{\text{cl}})$ in Section 4. $\boldsymbol{\theta}_{\text{rs}}$ are relevant only for AMI data, since they are used to model the radio-source contamination of the SZ cluster signal recorded by the SA, based on values measured with the LA. More information on the prior distributions used for $\boldsymbol{\theta}_{\text{rs}}$ can be found in Section 4.3 of P15.

3.3 Joint likelihood function

If one has an AMI dataset \mathbf{d}_{AMI} and a *Planck* dataset \mathbf{d}_{PI} , then the joint likelihood function for the data is given by

$$\mathcal{L}(\boldsymbol{\theta}) = \mathcal{L}(\mathbf{d}_{\text{AMI}}, \mathbf{d}_{\text{PI}}|\boldsymbol{\theta}, \mathcal{M}). \quad (2)$$

In this analysis we treat \mathbf{d}_{AMI} and \mathbf{d}_{PI} as being independent (see Section 5.3 for justification), and since the *Planck* predicted data only rely on the cluster parameters we can write

$$\mathcal{L}(\boldsymbol{\theta}) = \mathcal{L}_{\text{AMI}}(\mathbf{d}_{\text{AMI}}|\boldsymbol{\theta}, \mathcal{M}) \mathcal{L}_{\text{PI}}(\mathbf{d}_{\text{PI}}|\boldsymbol{\theta}_{\text{cl}}, \mathcal{M}). \quad (3)$$

3.3.1 AMI likelihood function

The AMI likelihood calculation is detailed in [Feroz et al. \(2009\)](#) (hereafter F09). Briefly, the AMI likelihood function $\mathcal{L}_{\text{AMI}}(\mathbf{d}_{\text{AMI}}|\boldsymbol{\theta}, \mathcal{M}) \equiv \mathcal{L}_{\text{AMI}}(\boldsymbol{\theta})$ is given by

$$\mathcal{L}_{\text{AMI}}(\boldsymbol{\theta}) = \frac{1}{Z_D} e^{-\frac{1}{2}\chi_{\text{AMI}}^2}. \quad (4)$$

Here χ_{AMI}^2 is a measure of the goodness-of-fit between the real and modelled data and can be expressed as

$$\chi_{\text{AMI}}^2 = \sum_{\nu, \nu'} \left[\mathbf{d}_{\text{AMI}, \nu} - \mathbf{d}_{\text{AMI}, \nu}^{\text{p}}(\boldsymbol{\theta}) \right]^{\text{T}} \mathbf{C}_{\text{AMI}, \nu, \nu'}^{-1} \times \left[\mathbf{d}_{\text{AMI}, \nu'} - \mathbf{d}_{\text{AMI}, \nu'}^{\text{p}}(\boldsymbol{\theta}) \right]. \quad (5)$$

In this expression $\mathbf{d}_{\text{AMI}, \nu}$ are the data observed by AMI at frequency ν , and $\mathbf{d}_{\text{AMI}, \nu}^{\text{p}}(\boldsymbol{\theta})$ are the predicted data generated by the model at the same frequency. $\mathbf{C}_{\text{AMI}, \nu, \nu'}$ is the theoretical covariance matrix for the AMI likelihood, which includes primordial CMB and source confusion noise as described in [Hobson and Maisinger \(2002\)](#) and F09 (Section 5.3). Source confusion noise allows for the remaining radio-sources with flux densities below the flux limit S_{lim} that the LA can subtract down to. The instrumental noise is estimated from the scatter of the visibility measurements within an observation. Referring back to equation 4, Z_D is a normalisation constant given by $(2\pi)^{D/2} |\mathbf{C}_{\text{AMI}}|^{1/2}$ where D is the length of \mathbf{d}_{AMI} (i.e. the combined vector of data from all frequencies).

3.3.2 Planck likelihood function

To calculate the *Planck* likelihood, we use a version of the PowellSnakes (PwS; [Carvalho et al. 2009](#) and [Carvalho et al. 2012](#)) Bayesian detection algorithm designed for detecting galaxy clusters in *Planck* data, adapted to operate on a previously determined position rather than to conduct a blind search. PwS treats the data observed by *Planck* as a superposition of background sky emission (including foreground emission and primordial CMB) \mathbf{b}_ν , instrumental noise \mathbf{n}_ν , and signal from the (cluster) source s_ν . The model for the predicted data vector is thus

$$\mathbf{d}_{\text{Pl},\nu}^{\text{p}}(\boldsymbol{\theta}_{\text{cl}}) = s_\nu(\boldsymbol{\theta}_{\text{cl}}) + \mathbf{b}_\nu + \mathbf{n}_\nu. \quad (6)$$

PwS works with patches of sky sufficiently small such that it can be assumed the noise contributions are statistically homogeneous. In this limit it is more convenient to work in Fourier space, as the Fourier modes are uncorrelated. It also assumes that the noise contributions are Gaussian, which is very accurate in the case of instrumental noise and the primordial CMB but may be more questionable for Galactic emission – the deviations from Gaussianity of \mathbf{b}_ν are discussed in Section 4.3 of [Carvalho et al. 2012](#). Since PwS is a detection algorithm, it calculates the ratio of the likelihood of detecting a cluster parameterised by $\boldsymbol{\theta}_{\text{cl}}$ and the likelihood of the data with no cluster signal ($s_\nu(\boldsymbol{\theta}_{\text{cl},0}) = 0$). Thus the log-likelihood ratio of the Fourier transformed quantities is

$$\ln \left[\frac{\mathcal{L}_{\text{Pl}}(\boldsymbol{\theta}_{\text{cl}})}{\mathcal{L}_{\text{Pl}}(\boldsymbol{\theta}_{\text{cl},0})} \right] = \sum_{\nu,\nu'} \tilde{\mathbf{d}}_{\text{Pl},\nu}^{\text{p}}(\boldsymbol{\theta}_{\text{cl}})^{\text{T}} \mathbf{C}_{\text{Pl},\nu,\nu'}^{-1} \tilde{\mathbf{d}}_{\text{Pl},\nu'}(\boldsymbol{\theta}_{\text{cl}}) - \frac{1}{2} \tilde{\mathbf{d}}_{\text{Pl},\nu}^{\text{p}}(\boldsymbol{\theta}_{\text{cl}})^{\text{T}} \mathbf{C}_{\text{Pl},\nu,\nu'}^{-1} \tilde{\mathbf{d}}_{\text{Pl},\nu}^{\text{p}}(\boldsymbol{\theta}_{\text{cl}}), \quad (7)$$

where tildes denote the Fourier transform of a quantity, and $\mathbf{C}_{\text{Pl},\nu,\nu'}$ is the covariance matrix of the data in Fourier space.

3.3.3 Joint likelihood analysis hyperparameters

Ideally when making a joint inference from two different datasets, likelihood hyperparameters would be used (see [Lahav et al. 2000](#), [Hobson et al. 2002](#), and [Ma and Berndsen 2014](#)) so that the relative weighting of the two likelihoods is treated in a Bayesian way. This allows meaningful results to be extracted when the datasets are not in good agreement, which could be due to, for example, systematic bias or an incorrect model. However the log-ratio given by equation 7 is not a probability density due to the fact that it is missing a normalisation factor proportional to $\tilde{\mathbf{d}}_{\text{Pl},\nu}^{\text{p}}(\boldsymbol{\theta}_{\text{cl}})^{\text{T}} \mathbf{C}_{\text{Pl},\nu,\nu'}^{-1} \tilde{\mathbf{d}}_{\text{Pl},\nu'}(\boldsymbol{\theta}_{\text{cl}})$. These hyperparameters affect the normalisation factor of the likelihood (it becomes a function of them), thus the PwS algorithm is incompatible with their use as it does not include the normalisation term in the likelihood calculations (a more detailed explanation is given in Chapter 8 of [Javid 2019](#)). We therefore do not include likelihood hyperparameters in our analysis. This should not be problematic when applying our method unless the data have been incorrectly analysed or the cluster model used is not flexible enough to describe both of the datasets.

4 CLUSTER MODEL

Since AMI and *Planck* observe the SZ effect caused by the electron gas in clusters (see e.g. [Birkinshaw 1999](#)), both telescopes measure signals proportional to the Comptonisation parameter y ,

$$y = \frac{\sigma_{\text{T}} k_{\text{B}}}{m_e c^2} \int T_e(r) n_e(r) dl, \quad (8)$$

where k_{B} is the Boltzmann constant, m_e is the rest mass of an electron, c is the speed of light, and σ_{T} is the Thomson scattering cross-section. $T_e(r)$ and $n_e(r)$ are respectively the electron temperature and number density in the intra-cluster medium, as a function of radius from the centre of the cluster (r), and the integral is over the line of sight. If an ideal gas equation of state is assumed for the electron gas then in terms of the electron pressure $P_e(r)$, the Comptonisation parameter is given by

$$y = \frac{\sigma_{\text{T}}}{m_e c^2} \int P_e(r) dl. \quad (9)$$

The cluster model considered here is used to calculate a ‘map’ of y by evaluating equation 9 at different points on the plane of the sky. It assumes a spherically symmetric, generalised-Navarro-Frenk-White (GNFW, [Nagai et al. 2007](#)) profile to model the electron pressure

$$P_e(r) = \frac{P_{\text{ei}}}{\left(\frac{r}{r_p}\right)^\gamma \left(1 + \left(\frac{r}{r_p}\right)^\alpha\right)^{(\beta-\gamma)/\alpha}}. \quad (10)$$

P_{ei} is an overall pressure normalisation factor and r_p is a characteristic radius.

The parameters α , β and γ describe the slope of the pressure profile at $r \approx r_p$, $r \gg r_p$ and $r \ll r_p$ respectively. Our model parameterises a cluster in terms of observational (rather than physical) quantities: θ_s , the characteristic angular scale corresponding to r_p ($\theta_s = r_p/D_A$ where D_A is angular diameter distance) and Y_{tot} , the total integrated Comptonisation parameter of the cluster, given by

$$Y_{\text{tot}} = \frac{4\pi\sigma_{\text{T}}}{m_e c^2} P_{\text{ei}} D_A \theta_s^3 \frac{\Gamma\left(\frac{3-\gamma}{\alpha}\right) \Gamma\left(\frac{\beta-3}{\alpha}\right)}{\alpha \Gamma\left(\frac{\beta-\gamma}{\alpha}\right)} \quad (11)$$

where Γ is the gamma function.

Our model therefore has input parameters $\boldsymbol{\theta}_{\text{cl}} = (x_0, y_0, Y_{\text{tot}}, \theta_s, \alpha, \beta, \gamma)$, where x_0 and y_0 are the cluster centre offsets from the designated central sky coordinate.

A set of ‘universal’ pressure profile (UPP) GNFW shape parameter values were derived in [Arnaud et al. \(2010\)](#) as the best fit to a sample of clusters from REXCESS (observed with XMM-Newton, [Böhringer et al. 2007](#)). These are $(\gamma, \alpha, \beta, c_{500}) = (0.3081, 1.0510, 5.4905, 1.177)$ and are often used as a fixed standard cluster profile. In this analysis we will not restrict our model profiles to the UPP case.

The GNFW profile extends to infinity; in practice some cut-off radius for the y -map must therefore be defined when implementing this model. A frequent choice, used for example in the analysis of *Planck* data, is to cut off at $\theta = 5\theta_{500} = 5\theta_s c_{500}$. For the case of the UPP, this implies that a spherical integral to $5\theta_{500}$ gives $Y_{\text{sph},5\theta_{500}} = 0.96 Y_{\text{tot}}$, or a cylindrical integral gives $Y_{\text{cyl},5\theta_{500}} = 0.97 Y_{\text{tot}}$ (with the line-of-sight integral extending to infinity within a radius of $5\theta_{500}$ on the sky). In the case of arbitrary values of (γ, α, β) , this fraction can change significantly; plus in the general case c_{500} is not necessarily known so a different cut-off radius must be defined which we denote θ_{lim} . We choose to define θ_{lim} for an arbitrary profile by the radius at which $Y_{\text{sph},\theta_{\text{lim}}} = 0.95 Y_{\text{tot}}$ (found via a numerical root-finder) by analogy with the UPP. For some profiles which fall off more slowly with radius this becomes prohibitively large and we therefore impose a maximum radius of $10\theta_s$. We have verified that in these cases the Comptonization parameter integrated over the line-of-sight at $10\theta_s$ is $< 0.1\%$ of the value at the centre, i.e. we are not cutting off substantial cluster signal in the outskirts.

We then translate the y -map to signal on the sky at each frequency using the non-relativistic approximation ([Zeldovich and](#)

Table 1. Cluster parameter prior distributions. \mathcal{N} denotes a Gaussian distribution parameterised by its mean and standard deviation, \mathcal{U} denotes a uniform distribution, and δ is a Dirac delta function. In the cases where the latter is used, the values used for the function’s argument will be stated when the analyses are carried out.

Parameter	Prior distribution(s)
x_0	$\mathcal{N}(0'', 300'')$
y_0	$\mathcal{N}(0'', 300'')$
Y_{tot}	$\mathcal{U}[0.00 \text{ arcmin}^2, 0.02 \text{ arcmin}^2]$
θ_s	$\mathcal{U}[1.3', 15']$
α	$\delta(\alpha_{\text{model}})$ or $\mathcal{U}[0.1, 3.5]$
β	$\delta(\beta_{\text{model}})$ or $\mathcal{U}[3.5, 7.5]$
γ	$\delta(\gamma_{\text{model}})$

Sunyaev 1969). Recently it has been shown that relativistic corrections may be significant for high-temperature clusters at *Planck* frequencies (e.g. Remazeilles et al. 2019); we note that relativistic effects *reduce* the *Planck* SZ signal, so if corrections were applied the effect would be to *increase* the discrepancy between AMI and *Planck* parameter constraints shown in P15.

4.1 Priors

In P15 we used a position prior based on the *Planck* position and error, and a joint ellipsoidal prior on Y_{tot} and θ_s based on the population of clusters detected by *Planck*. Here we assign wide, non-informative, independent priors to x_0 , y_0 , Y_{tot} and θ_s (see Table 1), to explore how much the combination of the two datasets can constrain the parameters.

In the standard *Planck* analysis and for the AMI data analysed in P15, the GNFw shape parameter values were fixed to the UPP values. In this analysis we will both simulate and analyse clusters with non-UPP profiles and explore the constraints on α and β produced by our joint dataset. The priors used for α and β vary throughout our analysis (Table 1); they are either fixed at some specific value (delta function priors) or allowed to vary uniformly (uniform priors on a bounded domain).

5 CLUSTER SIMULATIONS

For all simulations the y map of a single cluster is generated with ten distinct noise realisations as follows. Firstly, ten CMB realisations are created by sampling primordial CMB noise from an empirical power-law distribution (Hinshaw et al. 2013) and distributing at random positions on the sky. For each instrument, we add further realisations of the relevant sources of noise, as follows.

5.1 *Planck* cluster simulations

We construct a *Planck* all-sky foreground and thermal noise map by adding one noise realisation to the CO, FIRB, free-free, spinning dust, synchrotron and thermal dust emission maps simulated using the *Planck* sky model, all taken from the *Planck* Legacy Archive¹ using the FFP8 release. We note that we do not include point sources since as of this data release they were not separated into strong and weak point source maps, and for cluster analysis on real data the strong point sources would be masked. We also choose not to add the

thermal and kinetic SZ emission maps as we wish to see how much information can be extracted from the data in an ideal situation of a single, isolated cluster.

We then randomly select ten patch centres on the sky, with the constraint that the patch centres are above $\delta = 0^\circ$ (to satisfy AMI’s observing limits) and that all of the 20° square patch is outside of the *Planck* 20% Galactic plane mask (in which 20% of the sky is masked). We cut patches from the all-sky foreground + noise map at these coordinates and add the resulting patch maps to the CMB and cluster maps to produce the final *Planck* simulations. Each patch map therefore contains different thermal noise, foreground emission and CMB but the same cluster.

5.2 AMI cluster simulations

The AMI simulations are constructed by adding the cluster and CMB maps to confusion noise realisations, created using the 10C source counts given in AMI Consortium et al. (2011) up to a maximum flux density of $360 \mu\text{Jy}$ (i.e. assuming sources above $4\times$ a typical AMI-LA noise limit of $90 \mu\text{Jy}/\text{beam}$ have been detected and removed). A ten-hour mock AMI-SA observation is performed at the ten patch centres used for the *Planck* simulations, using the in-house package PROFILE (see e.g. Grainge et al. 2002). Instrumental noise is also added to the mock observations, giving a total noise level of $\approx 120 \mu\text{Jy}/\text{beam}$ on the map.

Similarly to the *Planck* simulations, each AMI simulation contains different thermal noise, confusion noise and CMB and the same cluster. Each AMI simulation corresponds directly to a *Planck* simulation which has the same observing centre and CMB realisation.

5.3 Testing the independence of the AMI and *Planck* datasets

In Section 3.3 we made the assumption that $d_{\text{AMI},\nu}^p$ and $d_{\text{PL},\nu}^p$ are not correlated with each other, so that the likelihoods for the two datasets can be separated. The instrumental noises associated with each telescope can safely be assumed to be independent. Due to the telescopes operating at different angular scales and frequencies, the confusion noise present in AMI data and foreground emission present in *Planck* data are assumed to be independent of one another. A similar argument can be applied for primordial CMB noise, nevertheless we carried out a simple test to see if this is the case. For a given set of cluster parameters, we ran the joint analysis on *Planck* and AMI datasets which had different CMB realisations to one another. We found that the resultant parameter constraints were not significantly different to the results obtained using AMI and *Planck* data which had the same CMB realisations as one another (Figure 1). We thus concluded that the covariance between the datasets introduced by the common CMB background was negligible.

6 CLUSTER SIMULATION RESULTS

In the following we apply the joint analysis to clusters simulated as described in Section 5, and compare results with analyses which use (the same) AMI or *Planck* data alone.

We consider simulations generated using three different sets of profile shape parameters: the UPP, the parameters fitted to a stacked *Planck* dataset in Planck Collaboration et al. (2013) (*Planck* Intermediate Profile’, PIP), and the parameters fitted to the cluster RXC J2319.6-7313 in Arnaud et al. (2010) which are the most different in the sample to the UPP (*REXCESS* Extreme Profile’, REP). These values are listed in Table 2. We consider a ‘low’

¹ <https://pla.esac.esa.int/#home>

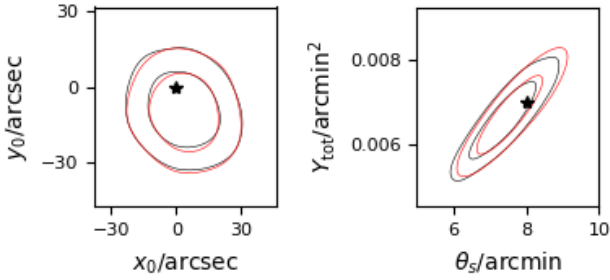


Figure 1. Two-dimensional marginalised x_0 - y_0 and Y_{tot} - θ_s posterior distributions for a high SNR (see Section 6) cluster simulation. The red contours correspond to the posterior distribution associated with the AMI and *Planck* datasets which had different CMB realisations to each other, while the black ones correspond to datasets generated with the same realisation. The star symbols indicate the values input when generating the simulations.

Table 2. Cluster simulation inputs using an observational model and three different pressure profile shapes. x_0 and y_0 are always 0, i.e. the cluster is at the simulated map centre.

		Y_{tot}	θ_s	γ	α	β
		/ arcmin ²	/ arcmin			
UPP	low SNR	0.001	2	0.3081	1.0510	5.4905
	high SNR	0.007	8			
PIP	low SNR	0.001	2	0.31	1.33	4.13
	high SNR	0.007	8			
REP	low SNR	0.001	2	0.065	0.33	5.49
	high SNR	0.007	8			

and a ‘high’ signal-to-noise ratio (SNR) cluster, which correspond to input values of $(Y_{\text{tot}}, \theta_s) = (0.001 \text{ arcmin}^2, 2 \text{ arcmin})$ and $(Y_{\text{tot}}, \theta_s) = (0.007 \text{ arcmin}^2, 8 \text{ arcmin})$ respectively. We note that ‘low’ and ‘high’ SNR are in relation to the *Planck* simulations rather than the AMI simulations, where they are both well detected. We then analyse the ten different noise realisations for each cluster using the priors given in Table 1 and plot the resulting posterior distributions using `GETDIST`².

6.1 Analysis with fixed profile parameters

We firstly analyse the high- and low-SNR UPP simulations using (γ, α, β) fixed to the correct, input values. Figs. 2 and 3 show the results of the simulation sets using AMI data only, *Planck* data only, and the two datasets combined. Each two-dimensional marginalised posterior distribution plot shows the 68% confidence contours for the 10 different noise realisations, with the input values marked with black stars.

In the case of the positional parameters, it is clear that the higher angular resolution of the AMI data means that it drives the posterior inferences, although the addition of the *Planck* data does improve the constraints slightly in the high-SNR case. This result is consistent for all following analyses, and we do not consider the x_0 and y_0 constraints any further.

Both AMI and *Planck* constraints are degenerate in the θ_s/Y_{tot} plane and previous results based on AMI and *Planck* data have relied

on ancillary data to reduce this degeneracy. For AMI, a correlated prior in θ_s and Y_{tot} based on a simulated population of clusters injected into and recovered from *Planck* data was used (see P15). For *Planck*, a prior on θ_s has been used to ‘slice’ the $\theta_{500}/Y(r_{500})$ posterior constraint based on either an X-ray measurement or a mass-observable scaling relationship (see, e.g. [Planck Collaboration et al. 2016](#)), both relying on the assumption of the ‘universal’ c_{500} . The combination of AMI and *Planck* data removes the need for these ancillary priors and produces a much tighter constraint on both θ_s and Y_{tot} since the degeneracy directions are different. This is most striking in the case of the low SNR cluster, but is also evident in the case of the high SNR cluster.

We next analyse the PIP and REP simulations keeping (γ, α, β) fixed to the UPP values in the analysis, i.e. we now have a mismatch between the cluster profiles used to produce and analyse the simulations. The two-dimensional posterior constraints on Y_{tot} and θ_s in this case are shown in Figs. 4 and 5. In the case of the PIP simulations, all of the constraints are offset from the true position; although the direction of the offset is mostly in θ_s so that the one-dimensional marginal constraint on Y_{tot} is not too badly offset it is clear that any method to reduce the degeneracy by slicing the posterior will be problematic. In the case of the REP simulations, the low-SNR cluster constraints are not too badly affected by the profile mismatch; this is because the change is to the inner part of the profile which is not well-resolved by either instrument. The high-SNR constraints however are significantly biased both in the two-dimensional plane and in the one-dimensional Y_{tot} plane.

6.2 Variable shape parameter analysis

We next consider the same set of simulations described in Section 6, but now allowing the GFW shape parameters α and β to vary in the analysis. We assign the uniform priors stated in Table 1 to α and β .

Figs. 6 and 7 show two-dimensional posterior constraints for a selection of parameter pairs for the UPP low- and high-SNR cluster simulations respectively. The two sets of simulations share some common features, as follows. The constraints on Y_{tot} are mostly driven by the *Planck* data, since the lower-resolution *Planck* data are most suited to measuring the total cluster signal while the interferometric AMI data relies on extrapolations to larger angular scales than are measured; the joint constraints are generally tighter than the *Planck*-only constraints and appear unbiased. There is a large degeneracy between θ_s and β which is inherent to the GFW model, since decreasing β makes the cluster amplitude fall off more slowly with radius which can also be achieved by increasing θ_s .

In the case of the low SNR cluster, the joint analysis successfully constrains Y_{tot} and puts an upper limit on θ_s and a lower limit on β . α is fairly unconstrained since it affects the profile on the scale of $\theta_s = 2 \text{ arcmin}$ which is not well-resolved by either instrument.

In the case of the high SNR cluster, α can be constrained by AMI alone. The joint analysis places a lower limit on θ_s but β is unconstrained due to the θ_s/β degeneracy.

We do not show all of the constraints produced for the PIP and REP simulations as they are qualitatively similar, with the following exceptions. Since β is lower for the PIP it effectively makes the cluster much more extended. The significance of the high SNR AMI detection becomes much lower and with α and β allowed to vary all of the parameters are essentially unconstrained, so the joint constraints become driven by the *Planck* data. Y_{tot} is well-constrained; a lower limit can be put on θ_s and an upper limit on β , while α is unconstrained. In the low SNR case, only Y_{tot} is well-

² <http://getdist.readthedocs.io/en/latest/>.

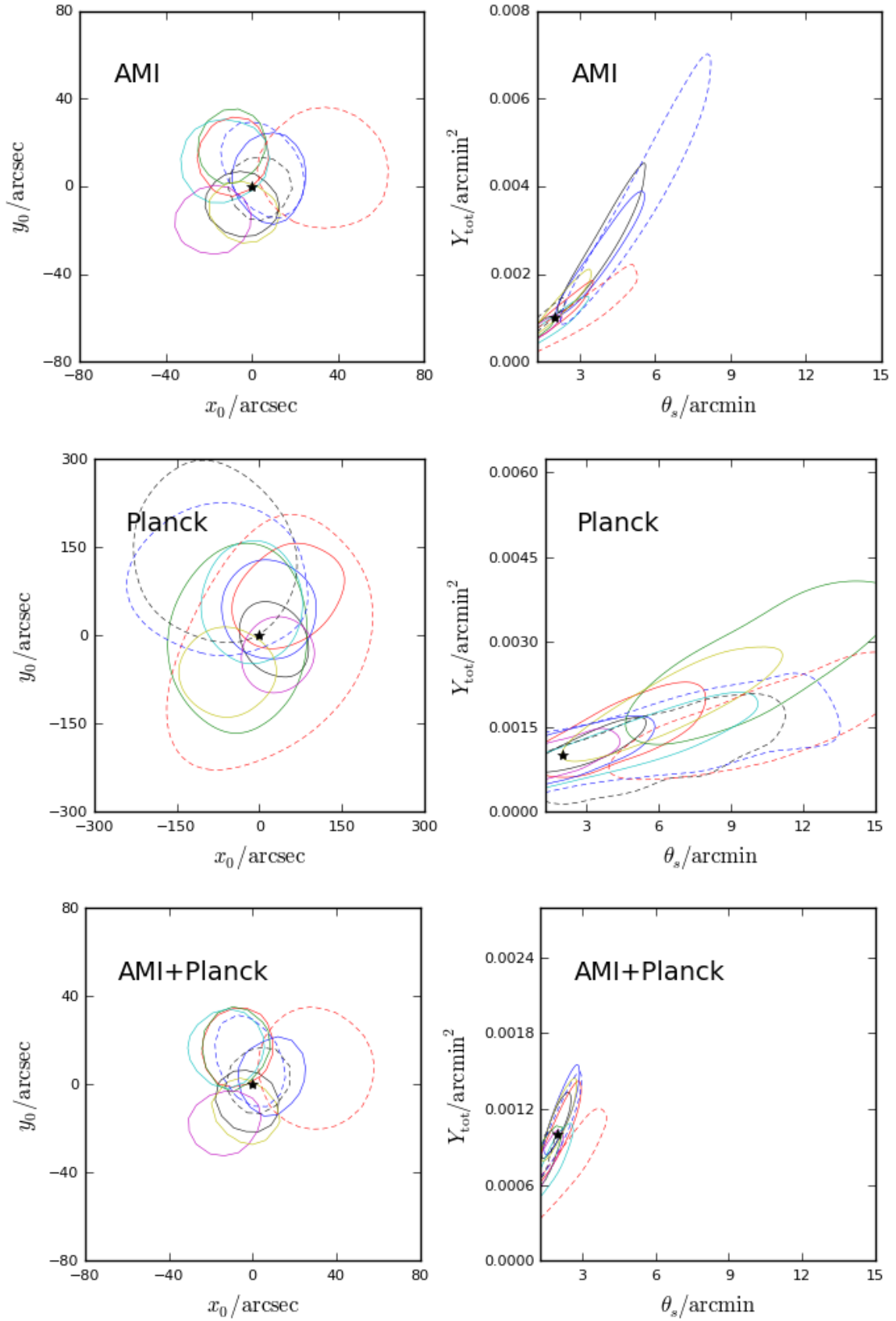


Figure 2. Two-dimensional marginalised x_0 - y_0 and Y_{tot} - θ_s posterior distributions for the 10 UPP low SNR cluster simulations obtained from: AMI data (top row), *Planck* data (middle row), and AMI and *Planck* data combined (bottom row). The contours in each plot represent the 68% confidence intervals of the separate posterior distributions obtained from each of the 10 realisations. The star symbols indicate the values input when generating the simulations. Note the different axis scales.

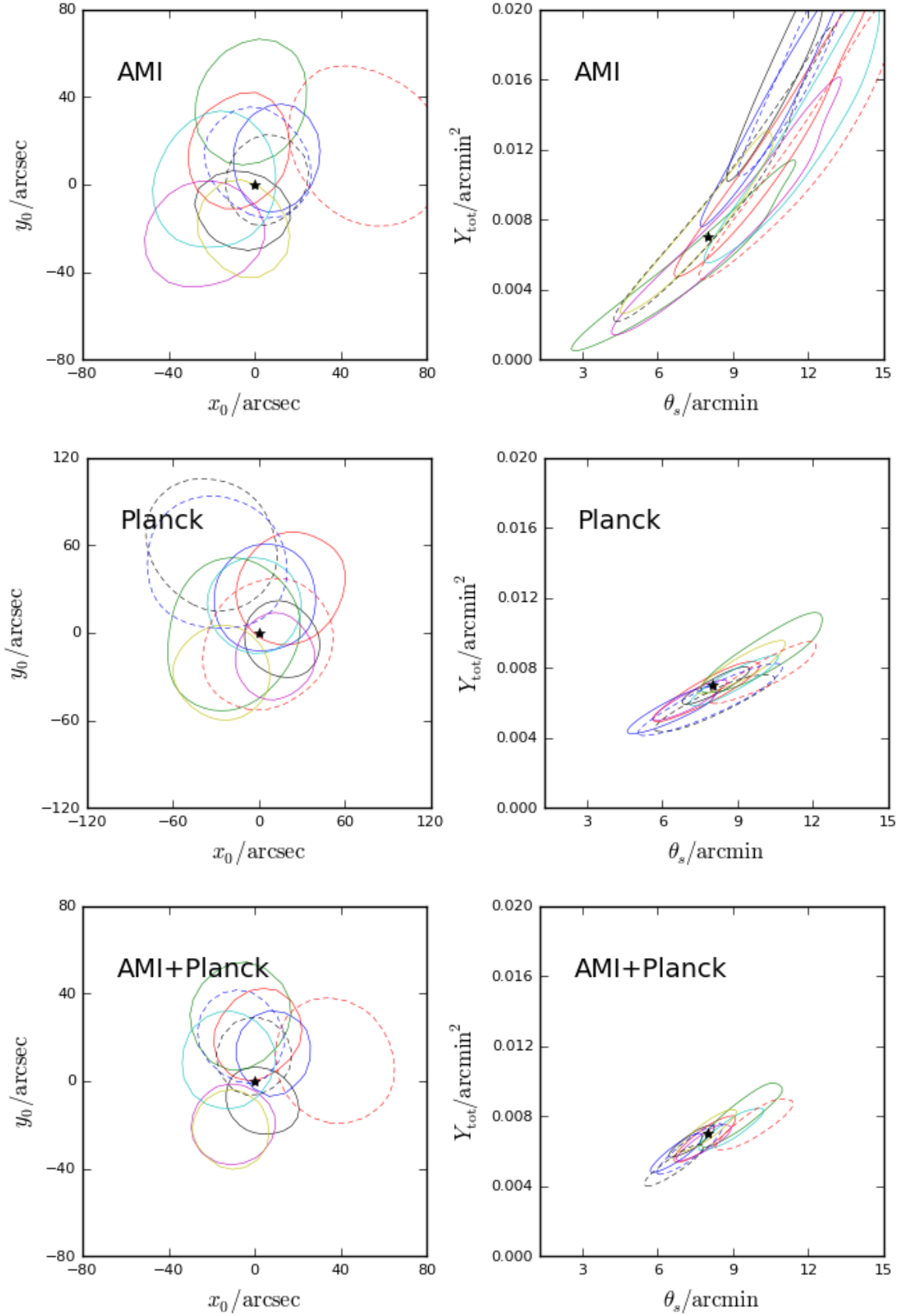


Figure 3. Two-dimensional marginalised x_0 - y_0 and Y_{tot} - θ_s posterior distributions for the 10 UPP high SNR cluster realisations. The Figure layout is as described in Figure 2. Note the different axis scales in the x_0 - y_0 plots.

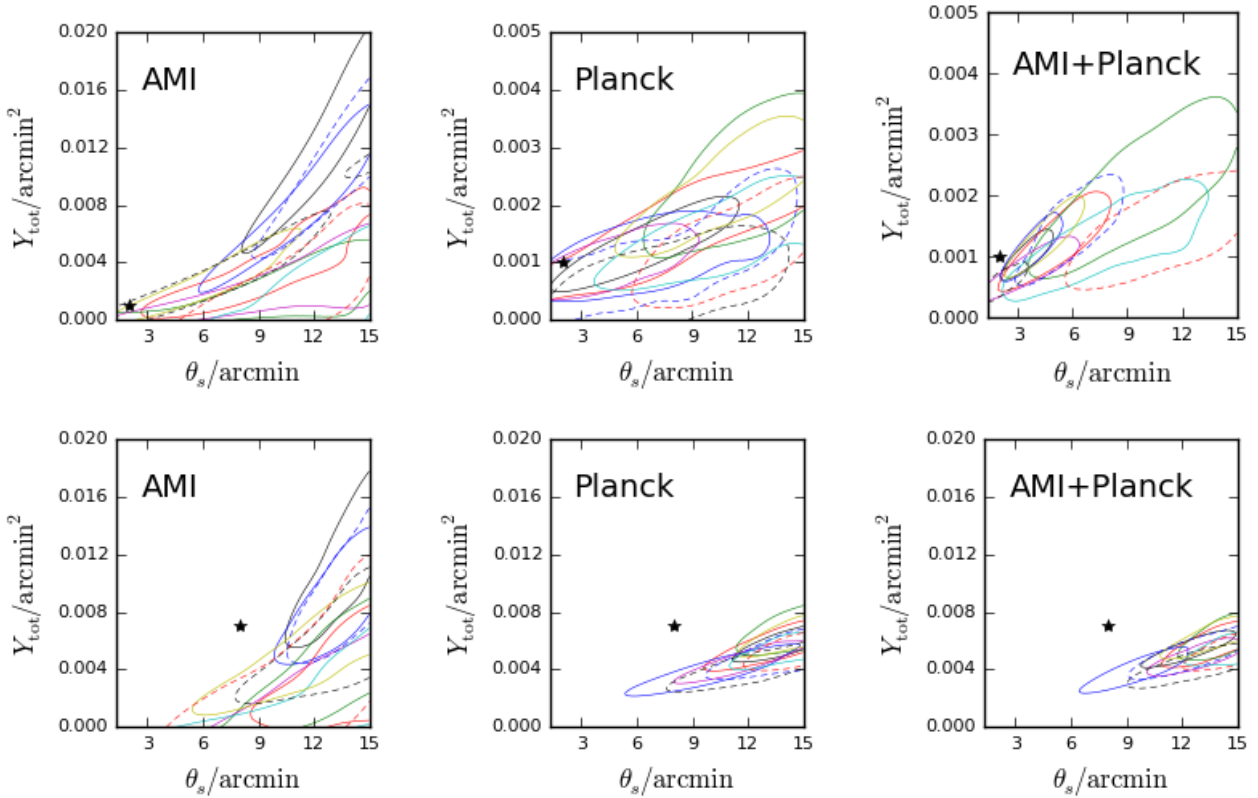


Figure 4. Two-dimensional marginalised $Y_{\text{tot}}-\theta_s$ posterior distributions for the 10 PIP low SNR cluster simulations (top row) and high SNR cluster simulations (bottom row). The posteriors plotted are, from left to right: AMI-only, *Planck*-only, and joint constraints. The contours and markers are as described in Figure 2. Note the different axis scales in the low-SNR plots.

constrained since although the cluster is more extended it is also much less bright so there is not enough signal-to-noise to constrain α and β . We show the joint constraints for this case in Fig. 8 as a ‘worst-case’ scenario.

In the high SNR, REP case, α is very tightly constrained and β is better-constrained by the AMI data alone. This is because the lower α value of the profile causes it to fall off more sharply with radius, putting more signal on AMI scales. In the low SNR, REP case we obtain tight constraints on Y_{tot} and α , a tight upper limit on θ_s and a lower limit on β . We show the joint constraints for this case in Fig. 8 as a ‘best-case’ scenario. We note that for the REP analysis we are fixing γ to the incorrect, UPP value; we also varied α and β while fixing γ to the correct, REP value which had little impact on the parameter constraints.

Overall we conclude that where nothing is known a-priori about the pressure profile of the cluster (other than that it follows a GFW shape), we can use the combination of AMI and *Planck* data to successfully constrain Y_{tot} ; often constrain α ; and sometimes put limits on β and θ_s depending on how well-resolved the cluster is (which depends both on θ_s and on α and β).

7 APPLICATION OF JOINT ANALYSIS TO REAL CLUSTER DATA

As a test case, we apply the joint analysis to PSZ2 G063.80+11.42 ($z = 0.426$; $M_{500,\text{SZ}} = 6.2 \times 10^{14} M_{\odot}$) from the P15 sample. The cluster is well-detected by both *Planck* (PwS signal-to-noise-ratio =

6.5) and AMI (Bayesian detection significance = 3.8) and there is a significant offset between the AMI and *Planck* posterior constraints on Y_{tot} and θ_s . The AMI radio-source environment is relatively clean. We reobserved the cluster with AMI to benefit from the improved performance of the new correlator, and use the DX11d data release with strong point sources masked (*Planck* Collaboration, priv. comm.) for the *Planck* data.

We firstly run the AMI and *Planck* analyses separately using the priors given in Table 1 (assigning delta priors to the GFW shape parameters at UPP values), to confirm the discrepancy. For comparison we also ran the AMI analysis with the P15 priors; these three sets of posterior chains are shown in Fig. 9. We note that the tighter positional constraint in the latter case is due to a degeneracy with a radio source flux near one edge of the cluster; when the wider positional prior is used the source flux is allowed to increase, broadening the cluster decrement and shifting the position of the cluster. This has little effect on the θ_s/Y_{tot} constraint. We see that the discrepancy is confirmed with the newer AMI data (and the AMI Bayesian detection significance increases to 6.0); the *Planck* θ_s/Y_{tot} constraint lies significantly above that produced by AMI.

We now analyse the PSZ2 G063.80+11.42 data while allowing α and β to vary. Figure 10 shows the resulting posterior distributions for the AMI-only, *Planck*-only and joint analysis methods. Similarly to the simulations, we see that Y_{tot} is well constrained by the joint analysis and the constraint is completely driven by the *Planck* data. The addition of AMI data improves the constraint on θ_s from an upper limit to a true constraint, and both α and β are constrained, although not tightly. The one-dimensional parameter constraints are

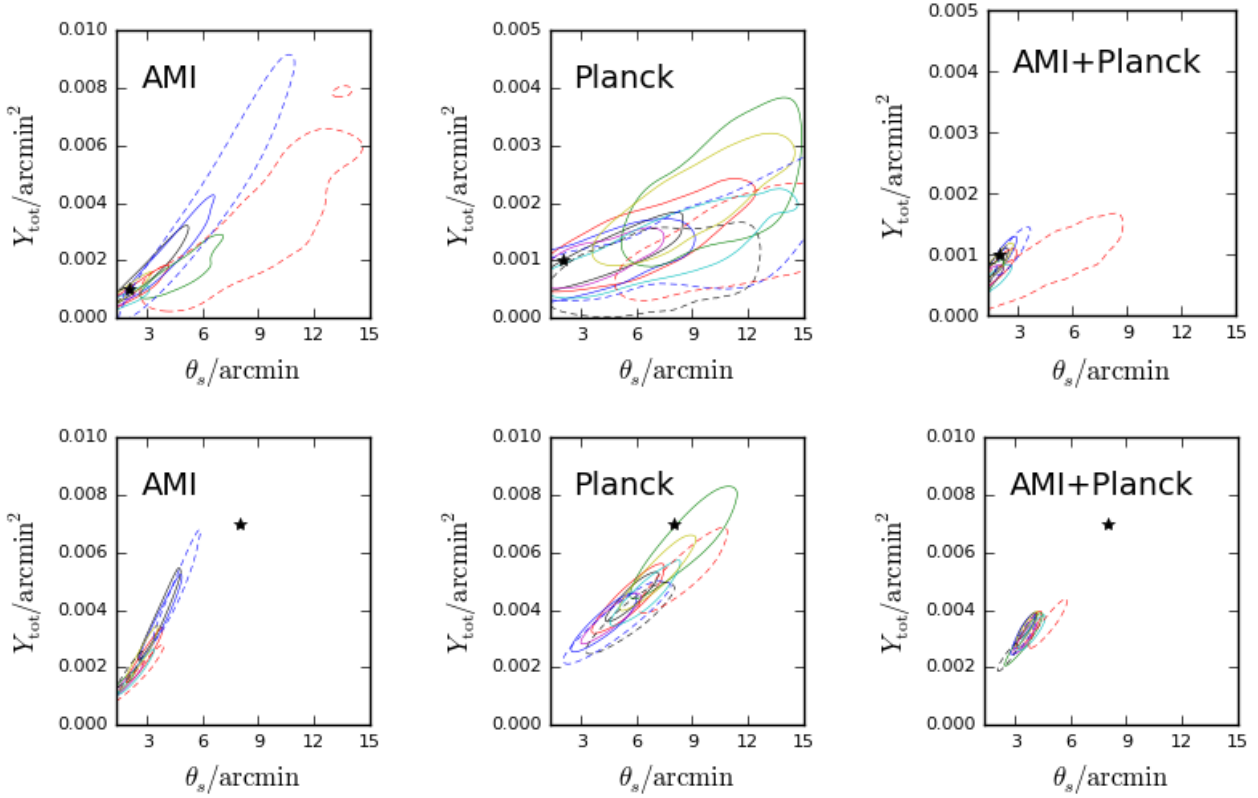


Figure 5. Two-dimensional marginalised $Y_{\text{tot}}-\theta_s$ posterior distributions for the 10 REP low SNR cluster simulations (top row) and high SNR cluster simulations (bottom row). The posteriors plotted are, from left to right: AMI-only, *Planck*-only, and joint constraints. The contours and markers are as described in Figure 2. Note the different y-axis scales.

Table 3. Summary of parameter constraints for PSZ2 G063.80+11.42, varying α and β . The errors given are the 68% limits from the one-dimensional marginalised parameter constraints.

	AMI-only	<i>Planck</i> -only	AMI- <i>Planck</i>
x_0 / arcsec	-59^{+24}_{-18}	-38^{+31}_{-26}	-55 ± 14
y_0 / arcsec	-70^{+26}_{-14}	-45 ± 31	-65 ± 15
Y_{tot} / (10^3 arcmin 2)	$6.9^{+2.3}_{-5.7}$	$1.32^{+0.17}_{-0.38}$	$1.40^{+0.23}_{-0.34}$
θ_s / arcmin	$8.9^{+3.9}_{-3.0}$	< 3.81	$4.27^{+0.95}_{-1.4}$
α	$0.77^{+0.10}_{-0.63}$	< 2.16	$1.66^{+0.55}_{-0.74}$
β	$4.79^{+0.42}_{-0.74}$	> 5.94	$5.78^{+1.0}_{-0.87}$

summarized in Table 3; β agrees with the UPP value, while a higher value of α is favoured but only at the $\approx 1\sigma$ level. We perform one further analysis on the AMI data, fixing α to the fitted value from the joint analysis, and leaving β fixed to the UPP value. The posterior constraints on θ_s and Y_{tot} in this case are shown in comparison with the AMI-only UPP analysis and the *Planck* analysis varying α and β ; it can be seen that the AMI posterior shifts in the correct direction to overlap with *Planck*, confirming that this value of α gives better agreement between the two instruments (Fig. 10, upper right-hand corner). No X-ray observations of this cluster are available to compare X-ray-derived constraints on the profile parameters; for our future AMI-*Planck* sample (see Section 8) comparison with X-ray-derived parameters will be informative and complementary across a different range of angular scales.

8 FUTURE WORK

Along with the sample of 99 clusters from P15, clusters which were previously excluded from the AMI sample due to difficult radio source environments are currently being reobserved with the new correlator; the superior dynamic range of the new instrument allows us to cope better with these environments and successfully extract cluster parameters. We will analyse all AMI detections with the joint pipeline, giving us a large cluster sample to probe deviations from the UPP and consider the impact this may have on the *Planck* cluster number counts.

We note that Javid et al. (2019) found that realistic radio source environments could bias the recovery of cluster parameters from AMI data. This issue and its effect on the recovery of the pressure profile parameters will be investigated in conjunction with the analysis of the larger AMI-*Planck* sample.

With the larger sample we will be able to compare our SZ-derived profile parameters to X-ray-derived parameters. This will allow us to test for any systematic differences and combine information across a broader range of angular scales.

Our pipeline is also simply extensible to the use of any physical model which uses a GNFW profile for the gas pressure, e.g. the models proposed in Olamaie et al. (2012), Javid et al. (2018) and Javid et al. (2019). We also plan to implement a non-parametric model such as that proposed in Olamaie et al. (2018).

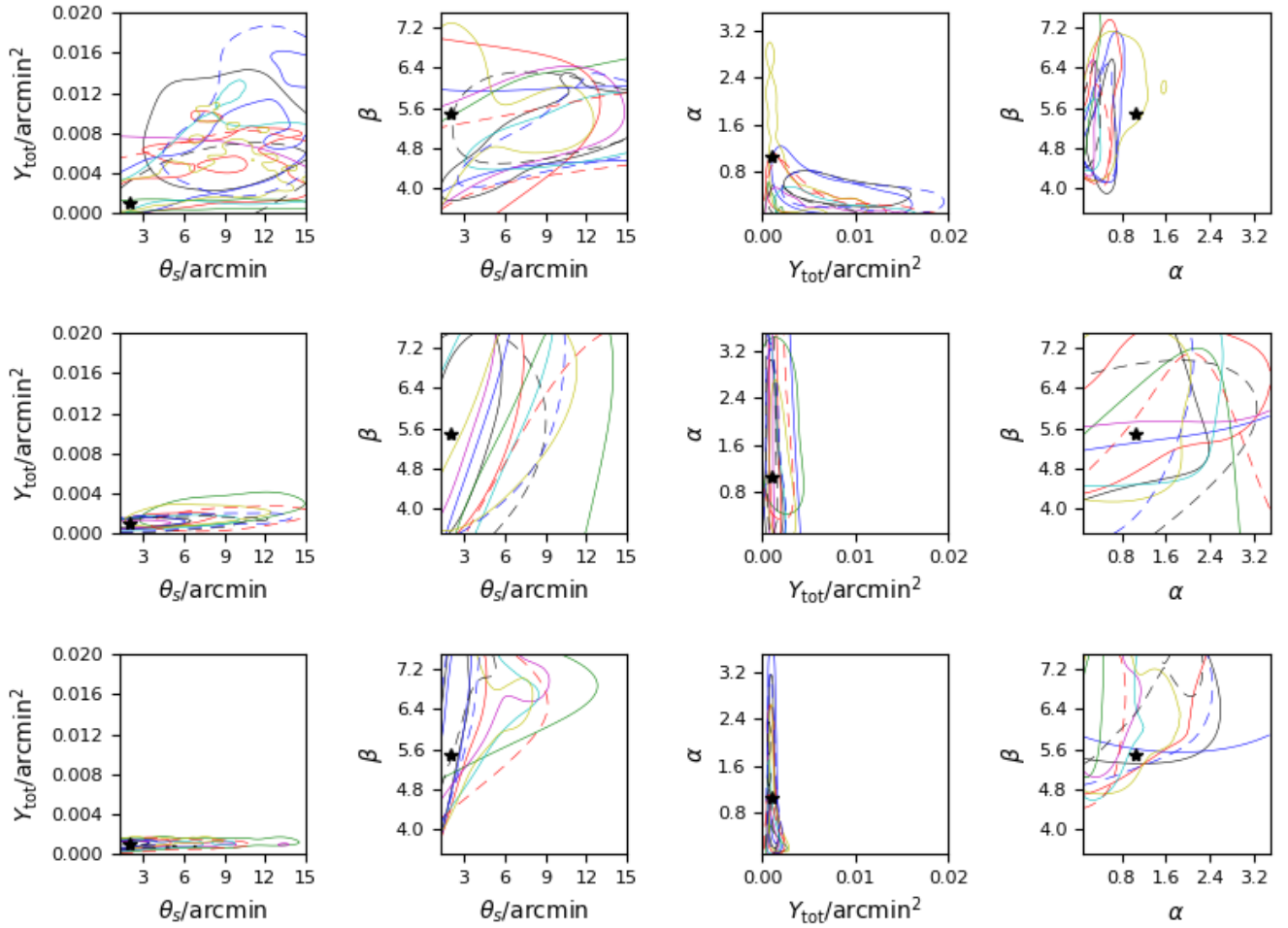


Figure 6. Two-dimensional marginalised posterior distributions for four combinations of θ_s , Y_{tot} , α and β , for the 10 UPP low SNR cluster simulations obtained from: AMI data (top row), *Planck* data (middle row), and AMI and *Planck* data combined (bottom row).

9 CONCLUSIONS

(i) We have developed a joint likelihood function for SZ data obtained from the *Planck* satellite and the Arcminute Microkelvin Imager (AMI) radio interferometer system, in order to compare inferences obtained using it with those from the individual likelihoods. The method could apply to any combination of *Planck* and interferometric data from one or more telescopes.

(ii) We generated simulations of clusters using an observational model similar to the one used in Perrott et al. (2015), using gas pressure profile shape parameter values taken from either the UPP (Arnaud et al. 2010, ‘universal’ pressure profile) or two other realistic variations. We considered both a smaller angular size, fainter cluster and a larger angular size, brighter cluster. From looking at the resulting posterior distributions we found the following:

- When *simulating* and *analysing* the clusters using the model with UPP parameters the joint analysis greatly reduced the degeneracy in $Y_{\text{tot}}-\theta_s$ shown in the individual AMI and *Planck* analyses, due to the different degeneracy directions for the individual datasets. The improvement on the parameter constraints for the joint analysis is particularly prominent in the small angular size cases. Thus when the profile shape of a cluster is known a-priori, the combination of the two datasets provides accurate, precise

constraints on the cluster parameters with no need for external information to reduce the $Y_{\text{tot}}-\theta_s$ degeneracy.

- When simulated clusters created using non-UPP profiles are analysed with the profile shape assumed to be UPP, the $Y_{\text{tot}}-\theta_s$ constraints are biased away from the true value. This occurs in the individual AMI and *Planck* datasets and is particularly problematic in the joint analysis, where a tight, significantly biased constraint is produced.

- When allowing the shape parameters to vary in the Bayesian analysis, we generally found that for all the clusters Y_{tot} was well-constrained and unbiased; *Planck* drove the constraint and the joint analyses improved the constraint slightly.

- Furthermore dependent on how well resolved the clusters are, the shape parameter α can often be constrained. Due to the strong $\beta-\theta_s$ degeneracy these parameters are more difficult to constrain and it is usually only possible to place limits on them.

(iii) Finally, we applied the joint analysis to real data for the cluster PSZ2 G063.80+11.42 which is part of the sample of 99 clusters considered in P15. We confirmed the discrepancy in Y_{tot} and θ_s estimates when using updated AMI data and resolved it by allowing α and β to vary. Using the joint analysis we could constrain Y_{tot} and θ_s well and place loose constraints on α and β , finding that

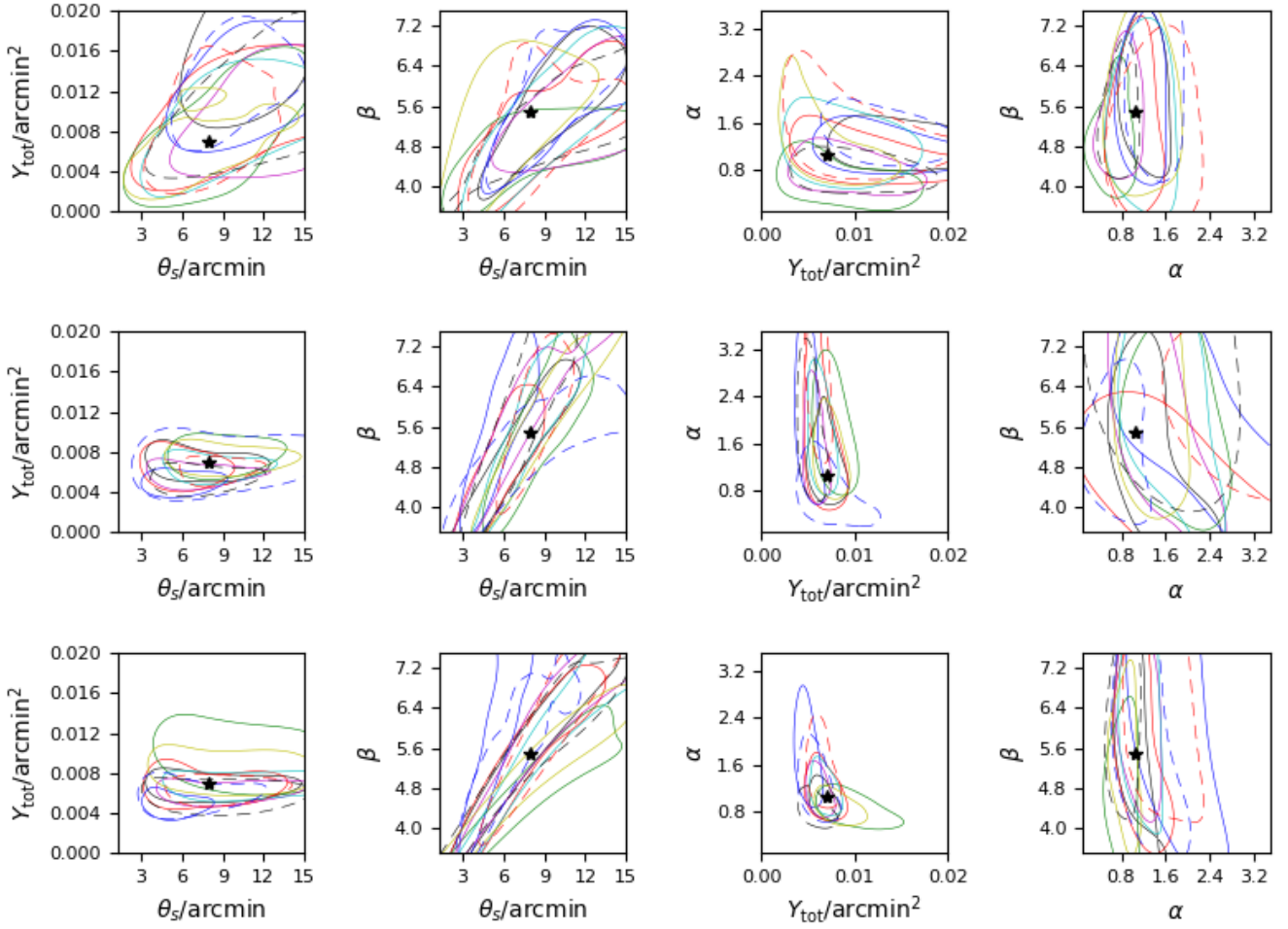


Figure 7. Two-dimensional marginalised posterior distributions for four combinations of θ_s , Y_{tot} , α and β , for the 10 UPP high SNR cluster simulations obtained from: AMI data (top row), *Planck* data (middle row), and AMI and *Planck* data combined (bottom row).

a slightly higher value of α than the UPP value was preferred, while the constraint on β was consistent with the UPP value.

(iv) We plan to apply our method to all the 99 clusters of the P15 sample, plus clusters currently being reobserved by AMI, to investigate deviations from the UPP and possible impact on the *Planck* cluster number counts. We also plan to extend our method to incorporate different physical and non-parametric cluster models.

ACKNOWLEDGEMENTS

We thank the staff of the Mullard Radio Astronomy Observatory for their invaluable assistance in the commissioning and operation of AMI, which is supported by Cambridge and Oxford Universities. This work is based on observations obtained with *Planck* (<http://www.esa.int/Planck>), an ESA science mission with instruments and contributions directly funded by ESA Member States, NASA, and Canada. This work was performed using the Darwin Supercomputer of the University of Cambridge High Performance Computing (HPC) Service (<http://www.hpc.cam.ac.uk/>), provided by Dell Inc. using Strategic Research Infrastructure Funding from the Higher Education Funding Council for England and funding from the Science and Technology Facilities Council. The

authors would like to thank Stuart Rankin from HPC and Greg Willatt and David Titterton from Cavendish Astrophysics for computing assistance. KJ and PJE acknowledge Science and Technology Facilities Council studentships. YCP acknowledges support from a Trinity College JRF and Rutherford Discovery Fellowship.

References

- Adam, R., and 39 colleagues 2015. Pressure distribution of the high-redshift cluster of galaxies CL J1226.9+3332 with NIKA. *Astronomy and Astrophysics* 576, A12.
- Adam, R., and 44 colleagues 2016. High angular resolution Sunyaev-Zel'dovich observations of MACS J1423.8+2404 with NIKA: Multi-wavelength analysis. *Astronomy and Astrophysics* 586, A122.
- Adam, R., and 37 colleagues 2014. First observation of the thermal Sunyaev-Zel'dovich effect with kinetic inductance detectors. *Astronomy and Astrophysics* 569, A66.
- Allen, S. W., Rapetti, D. A., Schmidt, R. W., Ebeling, H., Morris, R. G., Fabian, A. C. 2008. Improved constraints on dark energy from Chandra X-ray observations of the largest relaxed galaxy clusters. *Monthly Notices of the Royal Astronomical Society* 383, 879.
- AMI Consortium, and 18 colleagues 2012. Parametrization effects in the

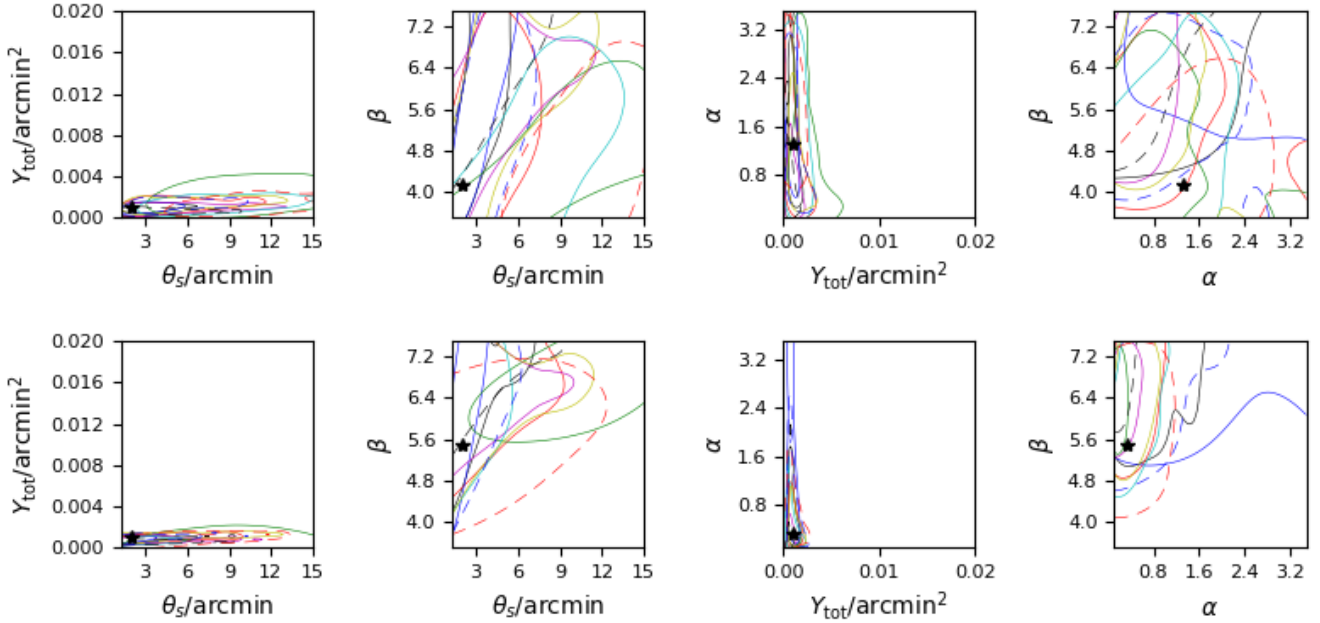


Figure 8. Two-dimensional marginalised posterior distributions for four combinations of θ_s , Y_{tot} , α and β , for the 10 PIP low SNR cluster simulations (top row) and REP low SNR cluster simulations (bottom row) obtained from AMI and *Planck* data combined. These represent our ‘worst-case’ and ‘best-case’ constraints for the set of clusters studied.

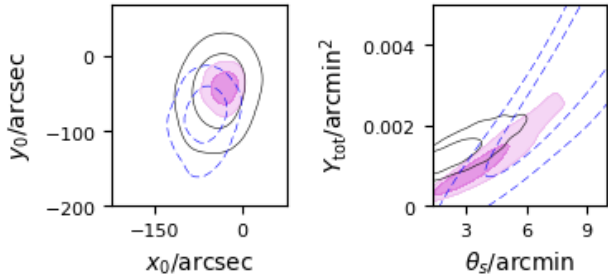


Figure 9. Posterior distributions for *Planck*-only (black, solid), AMI-only with flat priors (blue, dashed) and AMI-only with P15 priors (magenta, filled contours) analyses of PSZ2 G063.80+11.42, fixing the profile shape parameters at the UPP values. Note the range of the right-hand plot is truncated to better display the degeneracies.

analysis of AMI Sunyaev-Zel’dovich observations. *Monthly Notices of the Royal Astronomical Society* 421, 1136.

Arnaud, M., Pratt, G. W., Piffaretti, R., Böhringer, H., Croston, J. H., Pointecouteau, E. 2010. The universal galaxy cluster pressure profile from a representative sample of nearby systems (REXCESS) and the $Y_{\text{SZ}} - M_{500}$ relation. *Astronomy and Astrophysics* 517, A92.

Birkinshaw, M. 1999. The Sunyaev-Zel’dovich effect. *Physics Reports* 310, 97.

Bleem, L. E., and 73 colleagues 2015. Galaxy Clusters Discovered via the Sunyaev-Zel’dovich Effect in the 2500-Square-Degree SPT-SZ Survey. *The Astrophysical Journal Supplement Series* 216, 27.

Böhringer, H., and 33 colleagues 2007. The representative XMM-Newton cluster structure survey (REXCESS) of an X-ray luminosity selected galaxy cluster sample. *Astronomy and Astrophysics* 469, 363.

Carvalho, P., Rocha, G., Hobson, M. P. 2009. A fast Bayesian approach to discrete object detection in astronomical data sets - PowellSnakes I.

Monthly Notices of the Royal Astronomical Society 393, 681.

Carvalho, P., Rocha, G., Hobson, M. P., Lasenby, A. 2012. PowellSnakes II: a fast Bayesian approach to discrete object detection in multi-frequency astronomical data sets. *Monthly Notices of the Royal Astronomical Society* 427, 1384.

Chevallier, M., Polarski, D. 2001. Accelerating Universes with Scaling Dark Matter. *International Journal of Modern Physics D* 10, 213.

Czakon, N. G., and 13 colleagues 2015. Galaxy Cluster Scaling Relations between Bolocam Sunyaev-Zel’dovich Effect and Chandra X-Ray Measurements. *The Astrophysical Journal* 806, 18.

da Silva, A. C., Kay, S. T., Liddle, A. R., Thomas, P. A. 2004. Hydrodynamical simulations of the Sunyaev-Zel’dovich effect: cluster scaling relations and X-ray properties. *Monthly Notices of the Royal Astronomical Society* 348, 1401.

AMI Consortium, and 18 colleagues 2011. 10C survey of radio sources at 15.7 GHz - II. First results. *Monthly Notices of the Royal Astronomical Society* 415, 2708.

Di Mascolo, L., Churazov, E., Mroczkowski, T. 2019. A joint ALMA-Bolocam-Planck SZ study of the pressure distribution in RX J1347.5-1145. *Monthly Notices of the Royal Astronomical Society* 487, 4037.

Dutton, A. A., Macciò, A. V. 2014. Cold dark matter haloes in the Planck era: evolution of structural parameters for Einasto and NFW profiles. *Monthly Notices of the Royal Astronomical Society* 441, 3359.

Hasler, N., and 21 colleagues 2012. Joint Analysis of X-Ray and Sunyaev-Zel’dovich Observations of Galaxy Clusters Using an Analytic Model of the Intracluster Medium. *The Astrophysical Journal* 748, 113.

Herranz, D., and 6 colleagues 2002. Filtering techniques for the detection of Sunyaev-Zel’dovich clusters
 in multifrequency maps. *Monthly Notices of the Royal Astronomical Society* 336, 1057.

Einasto, J. 1965. On the Construction of a Composite Model for the Galaxy and on the Determination of the System of Galactic Parameters. *Trudy Astrofizicheskogo Instituta Alma-Ata* 5, 87.

Ettori, S., and 7 colleagues 2009. The cluster gas mass fraction as a cosmological probe: a revised study. *Astronomy and Astrophysics* 501, 61.

Feroz, F., Hobson, M. P., Bridges, M. 2009. MULTINEST: an efficient

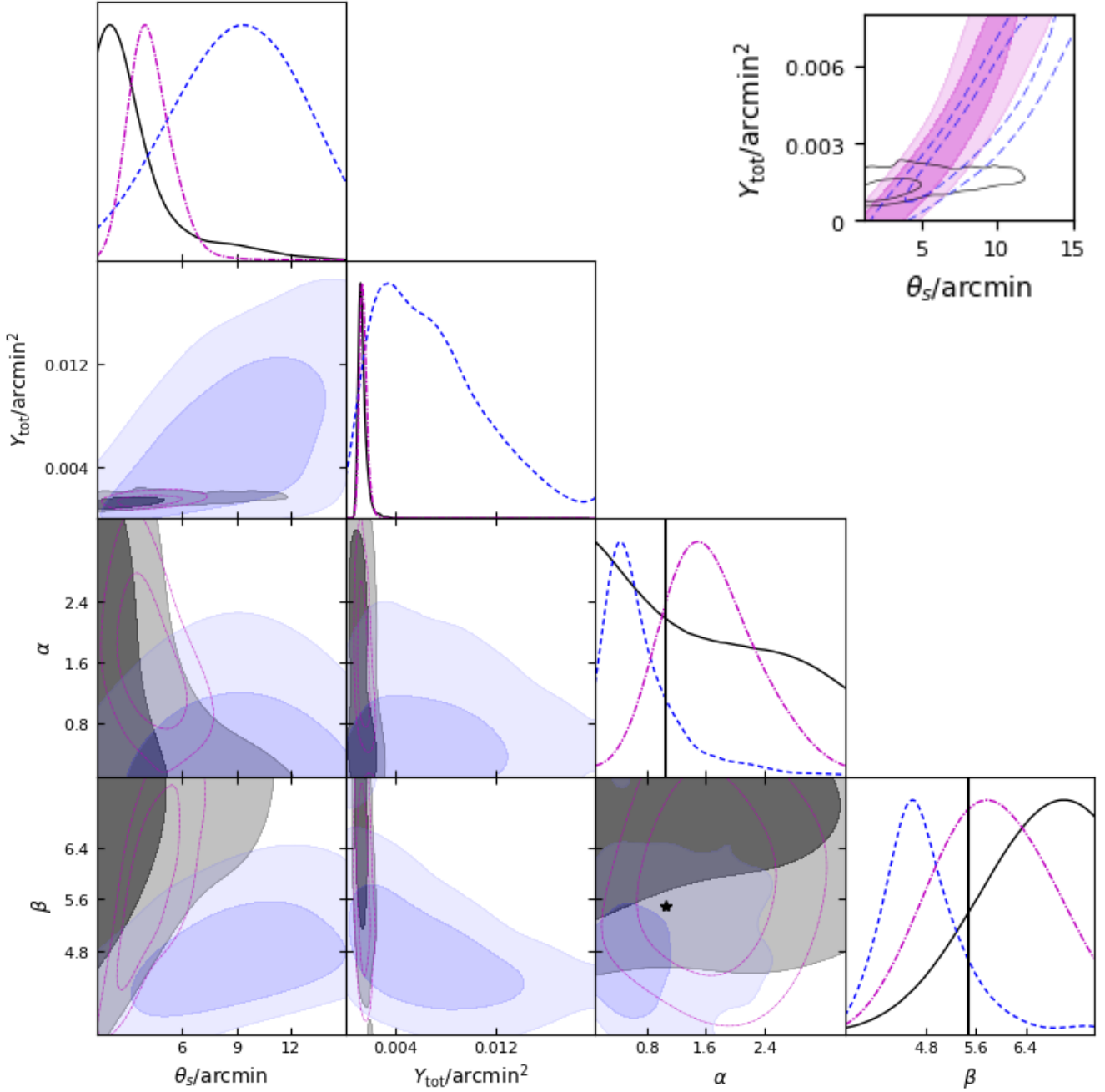


Figure 10. Bottom left-hand corner: triangle plot showing posterior distributions for *Planck*-only (black filled contours, solid lines), AMI-only (blue filled contours, dashed lines) and joint analysis (magenta empty contours, dot-dashed lines) of PSZ2 G063.80+11.42, all with the same priors, allowing α and β to vary. The black vertical lines and star show the UPP values of α and β . In the upper right-hand corner, the blue dashed and filled magenta contours show AMI-only analyses with α fixed to the UPP value and the joint analysis value (1.66), respectively; the posterior has shifted to better overlap with the *Planck*-only posterior with α and β varying, shown with solid black contours.

and robust Bayesian inference tool for cosmology and particle physics. *Monthly Notices of the Royal Astronomical Society* 398, 1601.

Feroz, F., Hobson, M. P., Zwart, J. T. L., Saunders, R. D. E., Grange, K. J. B. 2009. Bayesian modelling of clusters of galaxies from multifrequency-pointed Sunyaev-Zel'dovich observations. *Monthly Notices of the Royal Astronomical Society* 398, 2049.

Grange, K., and 6 colleagues 2002. Measuring the Hubble constant from Ryle Telescope and X-ray observations, with application to Abell 1413. *Monthly Notices of the Royal Astronomical Society* 333, 318.

Grange, K., and 7 colleagues 2015. The SKA and Galaxy Cluster Science with the Sunyaev-Zel'dovich Effect. *Advancing Astrophysics with the Square Kilometre Array (AASKA14)* 170.

Hickish, J., and 20 colleagues 2018. A digital correlator upgrade for the Arcminute MicroKelvin Imager. *Monthly Notices of the Royal Astronomical Society* 475, 5677, DOI:<https://doi.org/10.1093/mnras/sty074>.

Hilton, M., and 43 colleagues 2018. The Atacama Cosmology Telescope: The Two-season ACTPol Sunyaev-Zel'dovich Effect Selected Cluster

- Catalog. *The Astrophysical Journal Supplement Series* 235, 20.
- Hinshaw, G., and 20 colleagues 2013. Nine-year Wilkinson Microwave Anisotropy Probe (WMAP) Observations: Cosmological Parameter Results. *The Astrophysical Journal Supplement Series* 208, 19.
- Hobson, M. P., Bridle, S. L., Lahav, O. 2002. Combining cosmological data sets: hyperparameters and Bayesian evidence. *Monthly Notices of the Royal Astronomical Society* 335, 377.
- Hobson, M. P., Masinger, K. 2002. Maximum-likelihood estimation of the cosmic microwave background power spectrum from interferometer observations. *Monthly Notices of the Royal Astronomical Society* 334, 569.
- Javid K. 2019. Physical modelling of galaxy clusters and Bayesian inference in astrophysics (Doctoral thesis). University of Cambridge, DOI:<https://doi.org/10.17863/CAM.40616>.
- Javid, K., Perrott, Y. C., Hobson, M. P., Olamaie, M., Rumsey, C., Saunders, R. D. E. 2018. Comparison of physical and observational galaxy cluster modelling. arXiv e-prints arXiv:1805.01968, DOI:<https://doi.org/10.17863/CAM.38865>.
- Javid, K., Perrott, Y. C., Rumsey, C., Saunders, R. D. E. 2019. Physical modelling of galaxy cluster Sunyaev-Zel'dovich data using Einasto dark matter profiles. *Monthly Notices of the Royal Astronomical Society* 489, 3135, DOI:<https://doi.org/10.1093/mnr/stz2341>.
- Javid, K., and 7 colleagues 2019. Physical modelling of galaxy clusters detected by the Planck satellite. *Monthly Notices of the Royal Astronomical Society* 483, 3529, DOI:<https://doi.org/10.1093/mnr/sty3115>.
- Kitayama, T., and 14 colleagues 2016. The Sunyaev-Zel'dovich effect at 5": RX J1347.5-1145 imaged by ALMA. *Publications of the Astronomical Society of Japan* 68, 88.
- Kornigut, P. M., and 8 colleagues 2011. MUSTANG High Angular Resolution Sunyaev-Zel'dovich Effect Imaging of Substructure in Four Galaxy Clusters. *The Astrophysical Journal* 734, 10.
- Lahav, O., Bridle, S. L., Hobson, M. P., Lasenby, A. N., Sodr , L. 2000. Bayesian 'hyper-parameters' approach to joint estimation: the Hubble constant from CMB measurements. *Monthly Notices of the Royal Astronomical Society* 315, L45.
- LaRoque, S. J., and 6 colleagues 2006. X-Ray and Sunyaev-Zel'dovich Effect Measurements of the Gas Mass Fraction in Galaxy Clusters. *The Astrophysical Journal* 652, 917.
- Ma, Y.-Z., Berndsen, A. 2014. How to combine correlated data sets-A Bayesian hyperparameter matrix method. *Astronomy and Computing* 5, 45.
- Mantz, A., Allen, S. W., Ebeling, H., Rapetti, D. 2008. New constraints on dark energy from the observed growth of the most X-ray luminous galaxy clusters. *Monthly Notices of the Royal Astronomical Society* 387, 1179.
- Mantz, A., Allen, S. W., Rapetti, D., Ebeling, H. 2010. The observed growth of massive galaxy clusters - I. Statistical methods and cosmological constraints. *Monthly Notices of the Royal Astronomical Society* 406, 1759.
- Marriage, T. A., and 68 colleagues 2011. The Atacama Cosmology Telescope: Extragalactic Sources at 148 GHz in the 2008 Survey. *The Astrophysical Journal* 731, 100.
- Marriage, T. A., and 70 colleagues 2011. The Atacama Cosmology Telescope: Sunyaev-Zel'dovich-Selected Galaxy Clusters at 148 GHz in the 2008 Survey. *The Astrophysical Journal* 737, 61.
- Melin, J.-B., Bartlett, J. G., Delabrouille, J. 2006. Catalog extraction in SZ cluster surveys: a matched filter approach. *Astronomy and Astrophysics* 459, 341.
- Monfardini, A., and 34 colleagues 2014. Latest NIKA Results and the NIKA-2 Project. *Journal of Low Temperature Physics* 176, 787.
- Muchovej, S., and 15 colleagues 2011. Cosmological Constraints from a 31 GHz Sky Survey with the Sunyaev-Zel'dovich Array. *The Astrophysical Journal* 732, 28.
- Nagai, D. 2006. The Impact of Galaxy Formation on the Sunyaev-Zel'dovich Effect of Galaxy Clusters. *The Astrophysical Journal* 650, 538.
- Nagai, D., Kravtsov, A. V., Vikhlinin, A. 2007. Effects of Galaxy Formation on Thermodynamics of the Intracluster Medium. *The Astrophysical Journal* 668, 1.
- Navarro, J. F., Frenk, C. S., White, S. D. M. 1995. Simulations of X-ray clusters. *Monthly Notices of the Royal Astronomical Society* 275, 720.
- Olamaie, M., Hobson, M. P., Grainge, K. J. B. 2012. A simple parametric model for spherical galaxy clusters. *Monthly Notices of the Royal Astronomical Society* 423, 1534.
- Olamaie, M., Hobson, M. P., Grainge, K. J. B. 2013. Mass and pressure constraints on galaxy clusters from interferometric Sunyaev-Zel'dovich observations. *Monthly Notices of the Royal Astronomical Society* 430, 1344.
- Olamaie, M., and 7 colleagues 2018. Free-form modelling of galaxy clusters: a Bayesian and data-driven approach. *Monthly Notices of the Royal Astronomical Society* 481, 3853.
- Perrott, Y. C., and 41 colleagues 2015. Comparison of Sunyaev-Zel'dovich measurements from Planck and from the Arcminute Microkelvin Imager for 99 galaxy clusters. *Astronomy and Astrophysics* 580, A95.
- Planck Collaboration, and 277 colleagues 2015. Planck 2013 results. XXXII. The updated Planck catalogue of Sunyaev-Zeldovich sources. *Astronomy and Astrophysics* 581, A14.
- Planck Collaboration, and 275 colleagues 2014. Planck 2013 results. XXIX. The Planck catalogue of Sunyaev-Zeldovich sources. *Astronomy and Astrophysics* 571, A29.
- Planck Collaboration, and 217 colleagues 2013. Planck intermediate results. V. Pressure profiles of galaxy clusters from the Sunyaev-Zeldovich effect. *Astronomy and Astrophysics* 550, A131.
- Planck Collaboration, and 201 colleagues 2016. Planck 2015 results. XXII. A map of the thermal Sunyaev-Zeldovich effect. *Astronomy and Astrophysics* 594, A22.
- Planck Collaboration, and 235 colleagues 2016. Planck 2015 results. XXIV. Cosmology from Sunyaev-Zeldovich cluster counts. *Astronomy and Astrophysics* 594, A24.
- Planck Collaboration, and 259 colleagues 2016. Planck 2015 results. XXVII. The second Planck catalogue of Sunyaev-Zeldovich sources. *Astronomy and Astrophysics* 594, A27.
- Remazeilles M., Bolliet B., Rotti A., Chluba J. 2019. Can we neglect relativistic temperature corrections in the Planck thermal SZ analysis? *MNRAS*, 483, 3459.
- Romero, C. E., and 13 colleagues 2015. Galaxy Cluster Pressure Profiles, as Determined by Sunyaev-Zeldovich Effect Observations with MUSTANG and Bolocam. I. Joint Analysis Technique. *The Astrophysical Journal* 807, 121.
- Romero, C., and 39 colleagues 2018. A multi-instrument non-parametric reconstruction of the electron pressure profile in the galaxy cluster CLJ1226.9+3332. *Astronomy and Astrophysics* 612, A39.
- Ruppin, F., and 40 colleagues 2017. Non-parametric deprojection of NIKA SZ observations: Pressure distribution in the Planck-discovered cluster PSZ1 G045.85+57.71. *Astronomy and Astrophysics* 597, A110.
- Ruppin, F., and 39 colleagues 2018. First Sunyaev-Zel'dovich mapping with the NIKA2 camera: Implication of cluster substructures for the pressure profile and mass estimate. *Astronomy and Astrophysics* 615, A112.
- Sayers, J., and 16 colleagues 2013. Sunyaev-Zel'dovich-measured Pressure Profiles from the Bolocam X-Ray/SZ Galaxy Cluster Sample. *The Astrophysical Journal* 768, 177.
- Sayers, J., and 9 colleagues 2016. A Comparison and Joint Analysis of Sunyaev-Zel'dovich Effect Measurements from Planck and Bolocam for a Set of 47 Massive Galaxy Clusters. *The Astrophysical Journal* 832, 26.
- Sehgal, N., and 68 colleagues 2011. The Atacama Cosmology Telescope: Cosmology from Galaxy Clusters Detected via the Sunyaev-Zel'dovich Effect. *The Astrophysical Journal* 732, 44.
- Staniszewski, Z., and 43 colleagues 2009. Galaxy Clusters Discovered with a Sunyaev-Zel'dovich Effect Survey. *The Astrophysical Journal* 701, 32.
- The Planck Collaboration 2006. The Scientific Programme of Planck. arXiv e-prints astro-ph/0604069.
- Vikhlinin, A., and 10 colleagues 2009. Chandra Cluster Cosmology Project III: Cosmological Parameter Constraints. *The Astrophysical Journal* 692, 1060.
- Williamson, R., and 74 colleagues 2011. A Sunyaev-Zel'dovich-selected

- Sample of the Most Massive Galaxy Clusters in the 2500 deg² South Pole Telescope Survey. *The Astrophysical Journal* 738, 139.
- Zeldovich, Y. B., Sunyaev, R. A. 1969. The Interaction of Matter and Radiation in a Hot-Model Universe. *Astrophysics and Space Science* 4, 301.
- Zwart, J. T. L., and 60 colleagues 2008. The Arcminute Microkelvin Imager. *Monthly Notices of the Royal Astronomical Society* 391, 1545.
- Adam, R., and 49 colleagues 2017. Mapping the kinetic Sunyaev-Zel'dovich effect toward MACS J0717.5+3745 with NIKA. *Astronomy and Astrophysics* 598, A115.

This paper has been typeset from a $\text{\TeX}/\text{\LaTeX}$ file prepared by the author.